Assessing the Ensemble Smoother with Multiple Data Assimilation for Subsurface Fluvial Geothermal Systems

Song, Guofeng; Geiger, Sebastian; Voskov, Denis; Abels, Hemmo A.; Vardon, Philip J.

PROCEEDINGS, 50th Workshop on Geothermal Reservoir Engineering
Stanford University, Stanford, California, February 10-12, 2025
SGP-TR-229

Assessing the Ensemble Smoother with Multiple Data Assimilation for Subsurface Fluvial Geothermal Systems

Guofeng SONG[1], Sebastian GEIGER[1], Denis VOSKOV[1,2], Hemmo A. ABELS[1], Philip J. VARDON[1]

[1]Department of Geoscience & Engineering, Delft University of Technology, Stevinweg 1, 2628 CN Delft, Netherlands

[2]Department of Energy Science & Engineering, Stanford University, Stanford, CA 94305, USA

G.Song-1@tudelft.nl

Keywords: fluvial geothermal systems, geological modeling, Rapid Reservoir Modeling, DARTS, uncertainty quantification, model updating

ABSTRACT

Efficient geothermal resource development remains challenging due to inherent geological uncertainty and limited subsurface data. A proof-of-concept for a digital twin for a fluvial geothermal reservoir, similar to the Delft campus geothermal project, is presented. This digital twin has the aim to integrate geological scenario modeling, production simulation, uncertainty analysis, and data assimilation to mitigate operational risks, reduce maintenance costs, extend reservoir longevity, and enhance the overall sustainability of this project. In this contribution, we assess the efficiency of the ensemble smoother with multiple data assimilation (ESMDA) for subsurface property inversion of a fluvial geothermal system. First, we developed an efficient method that allows for the swift creation of multiple geological scenarios of channelized reservoir geometries, fully constrained to well information, using Rapid Reservoir Modeling (RRM). Next, we generated an ensemble containing multiple geological realizations for a given scenario representing the geothermal system using stochastic reservoir modelling. For a single scenario and its ensemble of stochastically generated property distributions, heat flow and production rates were simulated using the Delft Advanced Research Terra Simulator (DARTS). One of the ensemble members and its simulated production data were taken as the "truth" (or reference) case. ESMDA was then employed to invert the property distribution within the fluvial channels of all other ensemble members, using the "observed" temperature and pressure data along the injection and production well from the "truth" case. We also consider the presence of a monitoring borehole to analyze how additional monitoring data impacts the convergence of ESMDA. The simulation results of the posterior models demonstrated a significant reduction in root mean square error for temperature and pressure data which align more closely with the "observations" compared to the prior models. This outcome confirms the feasibility of applying ESMDA for data assimilation in fluvial geothermal systems, such as the Delft campus geothermal project.

1. INTRODUCTION

Direct-use geothermal heating is one of the key available low-carbon energy solutions (Lund and Toth, 2021). The Delft campus geothermal project (Geothermie Delft, https://geothermiedelft.nl/en/) was established with two objectives: First, to serve as a research platform for developing new scientific and engineering insights and methods, and, second, to provide thermal energy for the TU Delft campus and parts of the city of Delft (Vardon et al., 2024; Vardon et al., 2020). The project consists of a doublet system targeting the fluvial Lower Cretaceous Delft sandstone formation at a depth of approximately 2 km beneath the campus (Willems et al., 2020). The injection and production doublet wells have been completed and thermal energy production is expected to commence in 2025. The project incorporates a comprehensive scientific program, including the installation of fiber optic cables, extensive logging and coring programs, and a seismic monitoring network. All available data will be assimilated with reservoir modeling techniques to enhance the understanding of the reservoir architecture, streamline data acquisition, constrain production uncertainty, and enable reliable reservoir performance forecasts and optimization for informed decision-making during commercial geothermal operations (Voskov et al., 2024).

We propose a workflow for an open-source digital twin for geothermal reservoirs that can assimilate available data and can be used for quantifying and constraining the uncertainty in production temperature and rates (Song et al., 2024). This digital twin workflow includes the following elements a) Well logs and seismic data which are utilized to design multiple geologically-plausible reservoir models that capture possible geological scenarios using the Rapid Reservoir Modelling (RRM) software. RRM is a sketch-based modelling software that allows users to rapidly generate a wide range of geologically consistent models and scenarios in 3D (Jacquemyn et al., 2021). b) Different property distributions are assigned to the facies modelled in RRM to capture uncertainty in the petrophysical data. c) The Delft Advanced Research Terra Simulator (DARTS) is combined with machine learning techniques to create proxy models that enable fast simulations (Khait and Voskov, 2018). d) As new production and monitoring data becomes available, data assimilation techniques will be applied to update property distributions for each scenario. This iterative process of data assimilation will help users constrain geological and production uncertainties, both of which are key to optimizing operational strategies.

Data assimilation, as a significant component of the digital twin framework, integrates measurements with numerical simulations of flow and heat transfer to improve reservoir characterization (Evensen et al., 2022). Common data assimilation techniques include ensemble-based methods (Emerick and Reynolds, 2013), gradient-based approaches (Tian et al., 2024), and fully non-linear DA methods (Chen et al., 2014). Recently, the ensemble-based ensemble smoother with multiple data assimilation (ESMDA) has gained popularity for subsurface inversion problems (Chen et al., 2024; Mohsan et al., 2024; Seabra et al., 2024). Its iteration and inflated covariance matrices

enable more robust updates of the subsurface models. It is computationally efficient, flexible and capable of integrating multi-source data. Saifullin et al. (2024) combined a physics-based geomechanical proxy model with ESMDA to enhance subsurface permeability quantification by integrating vertical displacement measurements from fluid production and injection, which supports the informed decision-making in geothermal production and CO_2 sequestration. Wu et al. (2021) assimilated tracer data to invert 2D. Oudshoorn et al. (2024) utilized ESMDA to integrate electromagnetic and production data, updating conductivity distributions to improve reservoir-wide temperature forecasts.

To date, only a limited number of studies have explored the application of ESMDA to complex geothermal reservoirs, particularly for projects such as the Delft campus geothermal project. Addressing this gap is a key task for developing the subsurface geothermal digital twin. In this contribution, we evaluate the feasibility of ESMDA for complex fluvial geothermal reservoirs in a synthetic yet geologically plausible and hence challenging proof-of-concept. The reservoir model is constructed using scenario-based RRM and facies-controlled sequential Gaussian simulation (Li et al., 2021). Production simulations for the geothermal doublet under different property distributions are performed with the open-source simulator DARTS. They are combined with ESMDA to constrain geothermal uncertainty and improve the understanding of the porosity and permeability distribution in the subsurface reservoir.

The paper is organized as follows: the Methodology section presents the geological modeling approach, open-source DARTS, and ESMDA. The Results section demonstrates the simulation outcomes and uncertainty analysis of the geothermal doublet, followed by the evaluation of the data assimilation for the geothermal reservoir. The conclusions are provided in the final section.

2. METHODOLOGY

2.1 Geological Modeling

RRM is an open-source, sketch-based modeling tool with an intuitive interface that allows users to rapidly create 3D geologically consistent reservoir models from 2D sketches (Jacquemyn et al., 2021; Petrovskyy et al., 2023). It employs the concept of surface-based reservoir modeling, where geological architectures and heterogeneities are represented by surfaces that define enclosed volumes, or geological domains. RRM is specifically designed for applications in data-poor environments and has been successfully deployed to design and screen geological scenarios for CO_2 storage (Jackson et al., 2022) and geothermal energy production (Baird et al., 2024). Using RRM, templates representing individual layers of a fluvial geothermal reservoir are created based on constraints such as channel belt width, net-to-gross (NTG), and channel sinuosity. Using these constraints, a library of channel layer templates is constructed through a uniform experimental design. Random selection, extraction, and strict comparison with well log data are applied to identify possible reservoir layers. The selected channelized layers are stacked with overlaps to mimic subsurface sedimentary processes (Song et al., 2024). Figure 1 depicts the reservoir model for a fluvial geothermal system that is used as the reference (i.e., “truth” case) in this study. Facies values of 1 and 2 represent sand and mudstone facies, respectively. The reference scenario features mid-sinuosity channel belts with widths ranging from 200 to 500 meters, a thickness of 10 m, and an overall NTG of 50%.

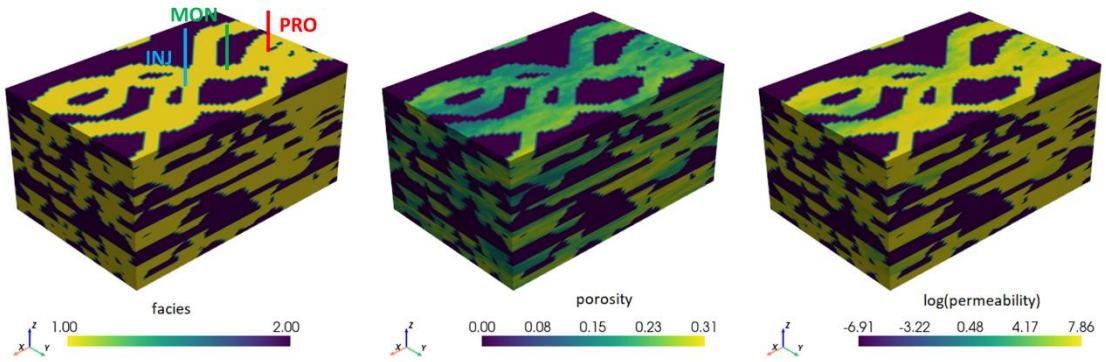

Figure 1: An example of a reservoir model for a channelized fluvial reservoir with its facies (1 = sand, 2 = mudstone), porosity, and permeability distributions (from left to right). Model dimensions are 3,000 m by 2,000 m by 120 m.

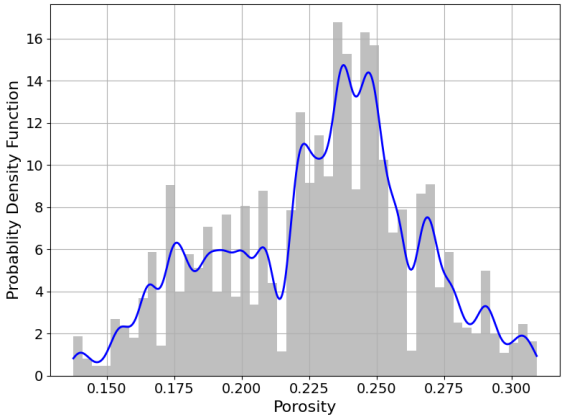

Figure 2: Probability density function of porosity in the sand facies of the reservoir model.

Facies-controlled sequential Gaussian simulation (SGSim) is employed to populate the porosity and permeability in the sand facies (Verly, 1993). Since the mudstones contribute minimally to advective heat transfer, its porosity is set to a constant value. Porosity and permeability from well logs are used as hard data for SGSim in the sand facies. A spherical model is used to fit the variogram function. Its porosity probability density function is presented in Figure 2. Permeability is computed using the following correlation (Willems et al., 2020)

$$\mathbf{log}_{10}(k) = -3.523\cdot 10^{-7}\cdot\phi^5 + 4.278\cdot 10^{-5}\cdot\phi^4 - 1.723\cdot 10^{-3}\cdot\phi^3 + 1.896\cdot 10^{-2}\cdot\phi^2 + 0.333\cdot\phi - 3.222\,. \tag{1}$$

2.2 Delft Advanced Research Terra Simulator

Since that the Delft campus geothermal project is a low-enthalpy geothermal system, we consider the standard governing equations for mass and energy conservation with thermal equilibrium assumptions between the solid and a single fluid phase. This study employs DARTS which employs a fully implicit solution in time and the finite volume method with a two-point flux approximation in space to discretize these governing equations. The conservation equations can be written as

$$\frac{\partial}{\partial t}(\phi\rho) - \nabla\cdot\rho v + \rho\tilde{q} = 0\,, \tag{2}$$

$$\frac{\partial}{\partial t}\left(\phi\rho U + (1-\phi)U_r\right) - \nabla\cdot h\rho v + \nabla\cdot(\kappa\nabla T) + h\rho\tilde{q} = 0\,, \tag{3}$$

where t is the time, ϕ is the porosity of porous media, ρ is the density of fluid phase, $\tilde{q}$ is the fluid rate per unit volume, U is the phase internal energy, U_r is the internal energy of rock, h is the convection coefficient and T is the temperature. The thermal conductivity of the fluid and rock is defined as

$$\kappa = \phi\kappa_f + (1-\phi)\kappa_r\,, \tag{4}$$

where κ, κ_r and κ_r are the thermal conduction coefficients of the overall system, the fluid phase, and the solid rock, respectively. The Darcy velocity v is given by

$$v = \frac{\mathbf{K}}{\mu}\left(\nabla p - \gamma_p\nabla D\right), \tag{5}$$

where $\boldsymbol{K}$ is the permeability of the porous media, μ is the fluid viscosity, p is the pressure, γ_p is the specific weight, and D is the depth.

We use pressure and enthalpy as primary variables and consider them the as state variables (Wang et al., 2020), which are evaluated using the Newton–Raphson method when solving for Equations (2) and (3)

$$\frac{\partial g(\boldsymbol{\omega}_k)}{\partial\boldsymbol{\omega}_k}\left(\boldsymbol{\omega}_{k+1} - \boldsymbol{\omega}_k\right) = -g(\boldsymbol{\omega}_k)\,. \tag{6}$$

Here, g represents the residual form of the governing equations, and the subscript k specifies the k-th nonlinear iteration. The Jacobian and residuals are computed via Operator-Based Linearization (Khait and Voskov, 2018; Voskov, 2017).

2.3 Ensemble Smoother with Multiple Data Assimilation (ESMDA)

ESMDA is utilized as the inversion methodology to estimate porosity and permeability fields in the channel sand of reservoirs. ESMDA extends the iterative ensemble smoother by introducing a set of inflation factors multiplied by the observation error covariance matrix. In this way, ESMDA controls the size of the updates at each iteration and reduces the risk of overfitting. ESMDA, as applied here, can be summarized by the following steps (Emerick and Reynolds, 2013):

1. Generate 100 prior realizations with heterogeneous properties for the specific scenario, setting the ensemble size *Ne* to 100.

$$\mathbf{M} = \left[\mathbf{m}_1, \mathbf{m}_2, \ldots, \mathbf{m}_i, \ldots \mathbf{m}_{Ne}\right], \tag{7}$$

where **M** refers to the porosity and permeability in all grid cells that contain the sand facies $\mathbf{m}_i = \begin{bmatrix} \phi \\ \mathbf{K} \end{bmatrix}_i$.

2. Define the key parameters in ESMDA. Set the number of iterations *Na* and the set of inflation factors $\boldsymbol{\alpha}$. The factors should satisfy the requirement $\sum_{l=1}^{Na} \frac{1}{\alpha_l} = 1$.

3. For all realizations, simulate heat and fluid flow from time zero by solving Equations (2) and (3) and obtain predictions at measurement locations across all time steps given by

$$\mathbf{d}_i^l = G\left(\mathbf{m}_i^l\right), \tag{8}$$

where $\mathbf{m}_i^l$ represents the porosity and permeability fields for the *i*-th member at iteration *l*. $G(\mathbf{x})$ is the forward model, i.e. the model that allows us to solve Equations (2) and (3).

4. For each ensemble member, perturb the measurement vector using $\mathbf{d}_{uc} = \mathbf{d}_{obs} + \sqrt{\alpha_l}\mathbf{C_D}^{1/2}\mathbf{z_d}$, where $\mathbf{z_d} \sim \mathcal{N}(0, \mathbf{I}_{Nd})$ and N_d is the total number of measurements assimilated. Here, $\mathbf{C_D}$ represents the measurement error covariance matrix. Update the parameter ensemble for the next iteration (*l*+1) using

$$\mathbf{m}_i^{l+1} = \mathbf{m}_i^{l+1} + \mathbf{C_{YD}}\left(\mathbf{C_{DD}} + \alpha_l \mathbf{C_D}\right)^{-1}\left(\mathbf{d}_{uc,i} - \mathbf{d}_i^l\right), i = 1, 2, \ldots, N_e, \tag{9}$$

where $\mathbf{C_{YD}}$ refers to the cross-covariance matrix between the model prediction and model parameters and $\mathbf{C_{DD}}$ to the covariance matrix of predicted data. Repeat steps 3 and 4 until the maximum number of iterations N_a is reached.

After the final iteration, the simulated production data at the wells is compared to the observed production data at the wells via the root mean square error (RMSE) to quantify the ensemble error relative to the reference values. A lower RMSE indicates better data assimilation performance

$$RMSE = \sqrt{\frac{1}{N}\sum_{i=1}^{N}\left(S_i - M_i\right)^2}, \tag{10}$$

where S_i is the estimated value and M_i is the true value.

3. RESULTS AND DISCUSSIONS

3.1 Production Analysis of a Fluvial Geothermal Doublet System

Our research is aimed at the Delft Sandstone, which is a channelized, clastic fluvial reservoir (Wang et al., 2021; Willems et al., 2020). Using the geological realizations generated with RRM and the fluid and reservoir properties from Wang et al. (2021), we construct a reservoir model approximating the geothermal doublet in this proof-of-concept study (Table 1). This model represents the reference geothermal system ("truth" case) for which we calculate production ("observed") data against which the simulation results for the model ensemble are compared. The reservoir top is at a constant depth of 2,000 m, with dimensions of 3,000 m × 2,000 m × 120 m. Porosity and permeability are constant for the mudstone facies. Their values are 0.01% and 0.001 mD, respectively. The porosity distribution in the sand facies is modelled using sequential Gaussian simulation, and permeability is calculated using Equation (1), as discussed above. In addition to the reference model, 100 equiprobable realizations are created, each with the same channel geometry as the reference model but different permeability and porosity distributions. This model ensemble represents the property uncertainty. The solid rock thermal conductivity and heat capacity are 259.2 kJ/m/day/K (3.0 W/m/K) and 2,450 kJ/m^3/K for the mudstone, respectively, and 190.8 kJ/m/day/K (2.2 W/m/K) and 2,300 kJ/m^3/K for the sand bodies, respectively. Initial reservoir temperature and pressure conditions are set to 353.15 K and 200 bar. The top and bottom boundaries are closed (i.e., no heat and fluid flow occurs across them), while all four lateral boundaries remain open to approximate an infinitely large aquifer with constant far-field temperature and pressure conditions. The reservoir contains three wells: one injection well, one production well, and one monitoring borehole. Note that a monitoring borehole is

scheduled to be drilled for the Delft campus geothermal project in 2028. The injection and production wells are spaced 1,200 m apart, with the monitoring borehole positioned midway between them. Each well extends 120 m vertically through the reservoir. Water is injected at a stable rate of 10,000 m^3/day at 298.15 K, while the production well extracts hot water at the same rate. The geothermal simulation was conducted over a 50-year period. The model is discretized into 40 m × 40 m × 1 m cells, resulting in a grid size of 75 × 50 × 120 with a total of 450,000 cells.

Table 1: Key parameters for the geothermal doublet.

Parameters	Values
Reservoir dimension	3,000 m × 2,000 m × 120 m
Injection-production spacing	1,200 m
Well length	120m
Porosity and k_h in mudstone facies	0.0001 and 0.001 mD
Porosity and k_h in sand facies	See Figure 2 and Equation (1)
k_v/k_h	0.1
Initial reservoir pressure and temperature	200 bar and 353.15 K
Solid rock conductivity, kJ/m/day/K	259.2 for the sand bodies, 190.08 for the mudstones
Solid rock heat capacity, kJ/m^3/K	2,450 for the sand bodies, 2,300 for the mudstones
Injection rate and temperature	10,000 m^3/day and 298.15 K

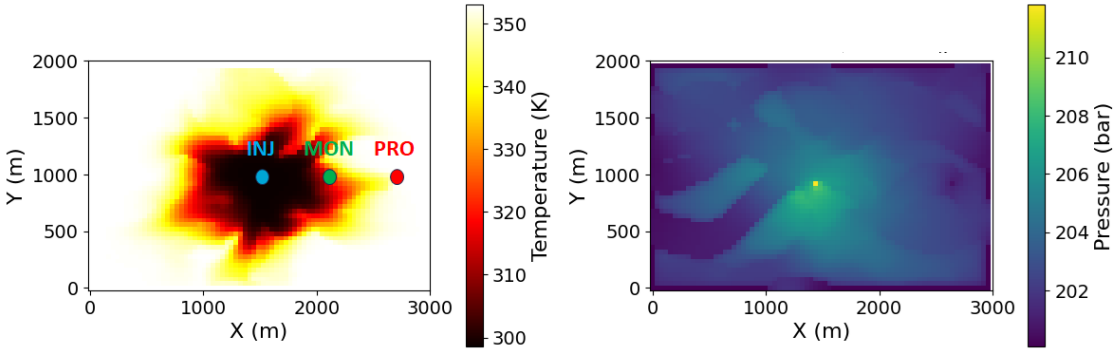

Figure 3: Map view of temperature (left) and pressure (right) distributions at a depth of 2,000 m after 25 years of production for the reference model. The dots in the left plot indicate the location of the injector and producer, and the monitoring borehole. Note that the injector location in the pressure distribution is visible in form of the maximum reservoir pressure. Some of the channels can be identified in the pressure distribution as well.

Figure 3 shows the areal temperature and pressure distributions after 25 years at the reservoir top surface (2,000 m depth). Both distributions show the impact of the high-permeability sands and the reduced flow in the mudstone facies. The sand bodies channel the cold water and lead to breakthrough. They are also the regions where pressure responses are more pronounced, indicating the presence of channelized sand bodies. Both, pressure and temperature distributions, are strongly impacted by diffusion (pressure diffusion and heat conduction, respectively) so the impact of the channels is less pronounced compared to two-phase flow processes (e.g., CO_2-brine displacement) or tracer transport. Still, the reservoir heterogeneity clearly impacts pressure distributions, thermal breakthrough, and flow patterns in the reservoir.

Figure 4 presents the simulated temperature and pressure profiles after 10, 20, and 30 years of production for the central monitoring borehole. The red line represents the reference data against which all other simulations are compared. The grey lines correspond to the 100 realizations from the model ensemble. The primary difference among different realizations arises from the different permeability and porosity distributions; hence the differences in the temperature profiles represent the reservoir uncertainty. The temperature profiles that are observed at the wells illustrate the dynamic evolution of reservoir during heat extraction. As the cold thermal plume gradually migrates away from the injection well, heat convection and conduction exhibit a highly transient behavior. The temperature profiles reflect the

layer properties: lower temperatures indicate rapid heat transfer, suggesting higher sand content between the injection and mid-well; conversely, higher temperatures indicate slower heat transfer and higher mud content. The profiles show that the upper layers (0 to 50 m) and lower layers (100 to 120 m) of the model have greater connectivity of the sand facies compared to the middle layers (50 to 100 m). Temperature profiles provide a broader characterization of the reservoir's overall layer properties. In contrast, the pressure profiles offer more insights about local facies in the near-wellbore region. Pressure remains relatively stable over time and is primarily influenced by permeability. In the sand facies in the vicinity of the monitoring borehole (e.g., depths of 0 to 24 m, 40 to 64 m, and 84 to 120 m), pressure increases with depth due to fluid flow from the upper to the lower layers. In contrast, in the mudstone facies (e.g., depths of 24 to 40 m and 64 to 84 m), the pressure profile represents the hydrostatic pressure since negligible flow occurs. Although the grey lines exhibit similar shapes, there are notable differences in the exact values, highlighting the variability among the porosity and permeability distributions. This variability, which represents the uncertainty in the production behavior, is more pronounced in the temperature profiles compared to the pressure profiles. For instance, after 20 years, the maximum temperature range reaches 36.92 K while the maximum pressure range is approximately 1.03 bar. The average ranges are 23.26 K and 0.74 bars, respectively. Given these uncertainties, data assimilation is necessary to reduce the variance and improve model reliability.

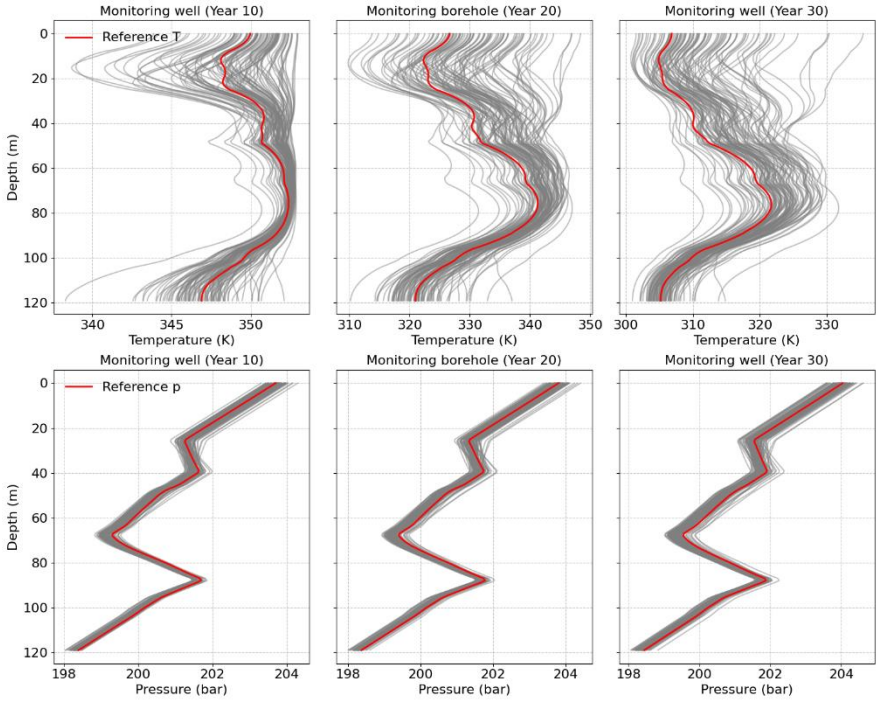

Figure 4: Temperature and pressure profiles as a function of depth at the central monitoring borehole after 10, 20, and 30 years of production. Thin grey lines show the forecasts from the model ensemble while the red lines show the "observed" reference temperature and pressure from the "truth" model.

3.2 Data Assimilation Analysis

During the ESMDA process, the observations are the temperature and pressure profiles from the injection well, the monitoring borehole, and the production well for the entire production period. The red curves in Figure 4 represent the reference data "observed" for the "truth" case at the monitoring borehole after 10, 20, and 30 years. Errors in this synthetic observation data are set to 2 K for temperature and 1 bar for pressure. Four iterations are performed with inflation factors [9.33, 7, 4, 2] using ESMDA. Only the properties within the channel are updated during data assimilation, since the mudstone facies are assumed to contribute minimally to flow processes and therefore its properties are set to be constant. As noted above, the ensemble size is 100, representing 100 reservoir models with heterogeneous porosity and permeability distributions. During each iteration, cell-specific porosity and permeability values are updated based on the difference between predictions from the previous iteration and perturbed observations (Equations 9).

Figures 5 and 6 show map views that illustrate the areal average property distributions for the prior and posterior ensemble, and the property distribution for the reference model at a depth of 2,010 m. Given the inherent uncertainty in the individual property distributions, ensemble averages are used for comparison. The results show that posterior porosity and permeability distributions, particularly around well locations, are closer to the reference than the prior distributions. These findings highlight ESMDA's capability to refine property distribution features, especially within the channel domain.

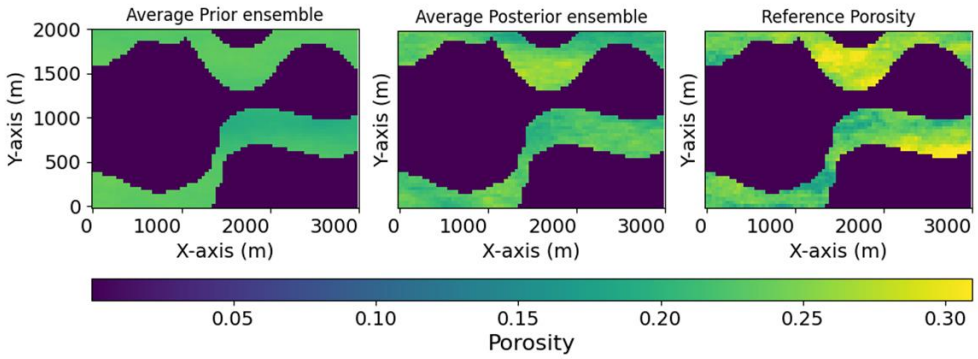

Figure 5: Map view of the areal average porosity distribution for the prior and posterior ensemble and the distribution for the reference model at a depth of 2,010 m.

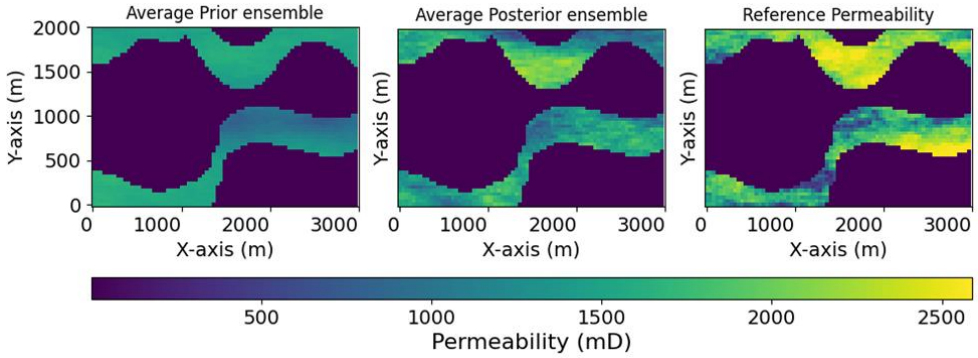

Figure 6: Map view of the areal average permeability distribution for the prior and posterior ensemble and the distribution for the reference model at a depth of 2,010 m.

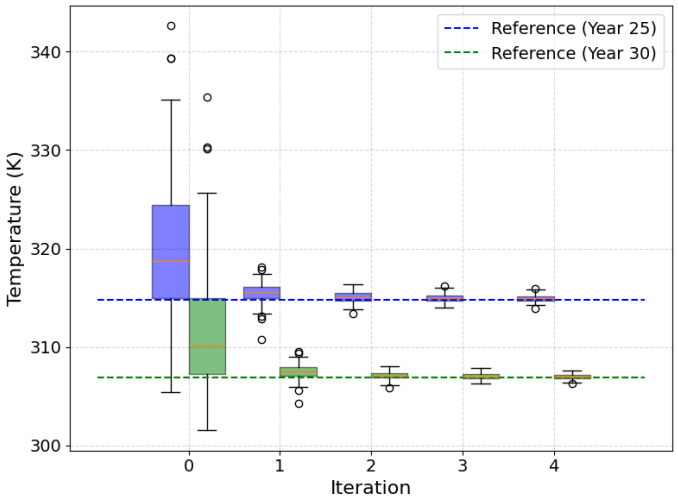

Figure 7: Comparison of temperature at an observation point (located at a depth of 2,000 m and areal coordinates of 1,000 m and 80 m) after 25 and 30 years with the reference values for different data assimilation iterations.

Figure 7 shows a box plot of the temperature values predicted after different data assimilation iterations for a randomly chosen observation point (depth of 2,000 m with areal coordinates of 1,000 m and 80 m). Outliers beyond the whiskers are displayed as circles. The orange line in each box indicates the median value of the 100 ensemble members while the purple and green dashed lines represent the reference ("observed") temperature values after 25 and 30 years of production. The prior ensemble exhibits larger errors relative to the reference data and hence higher uncertainty. As the iterations progress, the error decreases and the ensemble spread narrows. These results highlight ESMDA's capability to progressively constrain prediction uncertainty.

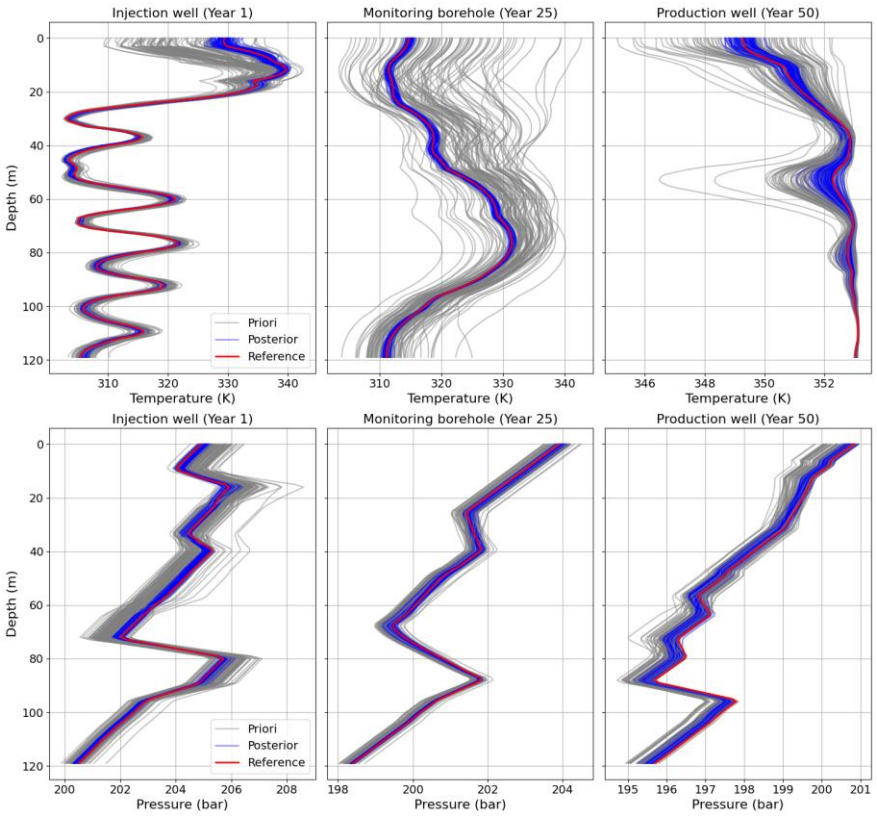

Figure 8: Prior, posterior and reference well temperature and pressure profiles recorded as a function of depth for the injection well, monitoring borehole and production well, after 1, 25, and 50 years of production, respectively (from left to right). The thin grey lines mean the prior forecasts, the red line denotes the observed reference data, and the blue lines are posterior predictions after data assimilation.

Figure 8 illustrates the prior predictions, posterior predictions, and reference data for the recorded along the injection and production wells and the monitoring borehole at different times. The selected variables include the injection well at year 1, the monitoring borehole at year 25, and the production well at year 50 – with the times selected to coincide where temperature variation is significant along a given well profile. After ESMDA, the posterior ensemble (blue curves) align much better to the "observed" data (red curves) compared to the prior ensemble (grey curves). The uncertainty of the posterior predictions is significantly better constrained. Take the temperature and pressure profiles at the monitoring borehole after 25 years of production as an example: the average temperature range at any depth is reduced from 24.37 K in the prior ensemble to 1.60 K in the posterior ensemble while the average pressure range is reduced from 0.80 to 0.34 bars. Table 2 provides the RMSE values for the temperature and pressure profiles for the prior and posterior at the different wells. The RMSE for temperature at the monitoring borehole decreases from 5.29 K in the prior ensemble to 0.31 K in the posterior ensemble, while the RMSE for pressure decreases from 0.18 to 0.09 bars.

Table 2: Average well temperature and pressure profiles RMSE for the injector and producer wells and monitoring borehole.

	Average temperature RMSE (K)		Average Pressure RMSE (bar)	
	Prior	Posterior	Prior	Posterior
Injection well	2.80	0.65	0.51	0.15
Monitoring borehole	5.29	0.31	0.18	0.09
Production well	0.54	0.16	0.30	0.20

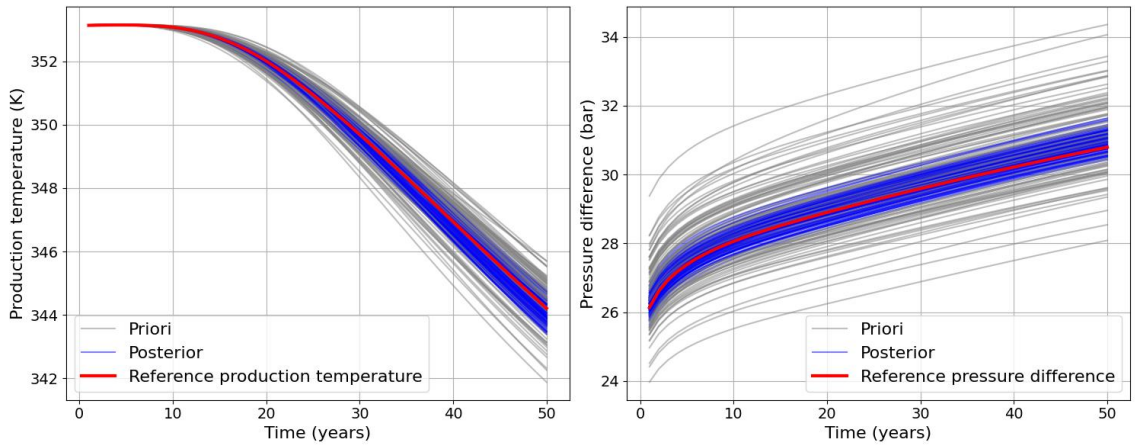

Figure 9: Comparison of prior and posterior production temperature and pressure differential.

Figure 9 compares the temporal evolution of the production temperature and pressure differentials between the producer and injector for the prior and posterior ensemble and the reference model ("truth" case). In this study, temperature and pressure profiles of three wells at different times are assimilated. Although we did not assimilate the production data, the posterior production temperature and pressure differential (blue curves) are closer to the "observed" reference data (red curve), exhibiting a lower variance and better constrained uncertainty. The production temperature range at the last year of operation decreases from 3.82 K to 1.40 K, and that of the pressure differential decreases from 6.3 to 1.2 bars. These results demonstrate the effectiveness of ESMDA in refining predictions, constraining uncertainty, and providing a more accurate estimate of reservoir dynamics.

4. CONCLUSIONS

We present a proof-of-concept study where we apply ESMDA to better constrain uncertainties in geothermal production data for a geologically complex geothermal reservoirs. Scenario-based RRM and facies-controlled sequential Gaussian simulations were used to construct a reference model ("truth" case) along with 100 additional realizations to capture uncertainties in porosity and permeability distributions. The open-source DARTS simulator enabled fast, high-fidelity thermal-hydraulic simulations. The realizations were input to ESMDA, using the simulated dynamic temperature and pressure profiles from injection, monitoring, and production wells as observations. Significantly better constrained uncertainties for permeability and porosity distributions and production forecasts were achieved.

In fluvial geothermal systems, the entire reservoir architecture, e.g. the channel geometry and property distributions, contributes to production uncertainties. In this study we focus only on the property distributions within the channels. It is observed that pressure and temperature profiles measured along the well paths at different times can provide valuable insights into reservoir performance and yield important data to improve production forecasts using ESMDA. Temperature profiles exhibit dynamic variations that are indicative of the fluid flow dynamics while pressure profiles remain relatively steady, reflecting permeability and reservoir connectivity.

ESMDA is shown to be a feasible method to constrain uncertainties in fluvial geothermal systems when assimilating temperature and pressure profiles recorded along the well trajectories. This indicates that ESMDA is likely applicable to the Delft campus geothermal project, with further optimization of DA parameters required in conjunction with more detailed geological models. ESMDA performance also depends on factors like ensemble size, iterations, and reliability of the observation data.

This research has several limitations. Only one geological scenario is utilized. However, in real-world conditions, multiple geological scenarios exist that could represent a subsurface reservoir, especially a channelized fluvial system. It is important to account for multiple geological scenarios, not just different property distributions, to capture a more realistic range of geological uncertainty. ESMDA can be combined with multiple geological scenarios to gradually narrow the scope of possible scenarios, enhancing the reliability of predictions in the future. Ensemble simulation results enable comprehensive uncertainty analysis by utilizing a catalog of scenarios rather than relying on a single deterministic model. The accuracy and reliability of the analysis depend on the ensemble size, which in this study consists of 100 realizations. Further sensitivity studies are necessary to determine the optimal ensemble size that adequately captures uncertainty. Additionally, incorporating more data types, such as fiber optics, electromagnetic measurements and transient data, into the data assimilation process can enhance the understanding of subsurface characterization. Since such data will become available for the Delft campus geothermal project, our approach can provide valuable insights into the value of information of different data types in constraining geological and production uncertainties and guide more effective data acquisition campaigns for future geothermal projects.

ACKNOWLEDGEMENTS

We thank the Delft University of Technology Excellence Foundation and Energi Simulation for supporting this study.

REFERENCES

Baird, K., Geiger, S., Hampson, G.J., et al.: Assessment of the Impacts of Multi-Scale Sedimentological Heterogeneity on Low-Enthalpy Geothermal Energy Production, 49th Stanford Geothermal Workshop, Stanford University, Stanford, CA (2024).

Chen, C., Deng, Y., Ma, H., et al.: Deep learning-based inversion framework by assimilating hydrogeological and geophysical data for an enhanced geothermal system characterization and thermal performance prediction, Energy, 302, (2024), 131713.

Chen, M., Tompson, A.F., Mellors, R.J., et al.: An efficient Bayesian inversion of a geothermal prospect using a multivariate adaptive regression spline method, Applied Energy, 136, (2014), 619-627.

Emerick, A.A.and Reynolds, A.C.: Ensemble smoother with multiple data assimilation, Computers & Geosciences, 55, (2013), 3-15.

Evensen, G., Vossepoel, F.C.and Van Leeuwen, P.J.: Data assimilation fundamentals: A unified formulation of the state and parameter estimation problem. Springer Nature, (2022).

Jackson, W.A., Hampson, G.J., Jacquemyn, C., et al.: A screening assessment of the impact of sedimentological heterogeneity on CO2 migration and stratigraphic-baffling potential: Johansen and Cook formations, Northern Lights project, offshore Norway, International Journal of Greenhouse Gas Control, 120, (2022), 103762.

Jacquemyn, C., Pataki, M.E., Hampson, G.J., et al.: Sketch-based interface and modelling of stratigraphy and structure in three dimensions, Journal of the Geological Society, 178(4), (2021), jgs2020-2187.

Khait, M.and Voskov, D.: Operator-based linearization for efficient modeling of geothermal processes, Geothermics, 74, (2018), 7-18.

Li, L., Qu, J., Wei, J., et al.: Facies-controlled geostatistical porosity model for estimation of the groundwater potential area in Hongliu Coalmine, Ordos Basin, China, ACS omega, 6(15), (2021), 10013-10029.

Lund, J.W.and Toth, A.N.: Direct utilization of geothermal energy 2020 worldwide review, Geothermics, 90, (2021), 101915.

Mohsan, M., Vossepoel, F.C.and Vardon, P.J.: On the use of different data assimilation schemes in a fully coupled hydro-mechanical slope stability analysis, Georisk: Assessment and Management of Risk for Engineered Systems and Geohazards, 18(1), (2024), 121-137.

Oudshoorn, C., Werthmüller, D., Slob, E., et al.: Numerical experiment on data assimilation for geothermal doublets using production data and electromagnetic observations, Geophysics, 89(6), (2024), M227-M237.

Petrovskyy, D., Jacquemyn, C., Geiger, S., et al.: Rapid flow diagnostics for prototyping of reservoir concepts and models for subsurface CO2 storage, International Journal of Greenhouse Gas Control, 124, (2023), 103855.

Saifullin, I., Seabra, G.S., Pluymakers, A., et al.: Integrating geomechanical proxy models with data assimilation for energy transition applications, Geomechanics for Energy and the Environment, (2024), 100618.

Seabra, G.S., Mücke, N.T., Silva, V.L.S., et al.: AI enhanced data assimilation and uncertainty quantification applied to Geological Carbon Storage, International Journal of Greenhouse Gas Control, 136, (2024), 104190.

Song, G., Geiger, S., Abels, H., et al.: Towards a Subsurface Geothermal Digital Twin: Efficient Construction of Geological Scenarios for Modelling Fluvial Geothermal Reservoirs, Fifth EAGE Global Energy Transition Conference & Exhibition (GET 2024), (2024).

Tian, X., Volkov, O.and Voskov, D.: An advanced inverse modeling framework for efficient and flexible adjoint-based history matching of geothermal fields, Geothermics, 116, (2024), 102849.

Vardon, P., Abels, H., Barnhoorn, A., et al.: A research and energy production geothermal project on the TU Delft campus: Project implementation and initial data collection, 49th Stanford Geothermal Workshop, Stanford University, Stanford, CA (2024).

Vardon, P., Bruhn, D., Steiginga, A., et al.: A geothermal well doublet for research and heat supply of the TU Delft Campus, World Geothermal Congress (2020).

Verly, G., 1993. Sequential Gaussian simulation: a Monte Carlo method for generating models of porosity and permeability, Generation, Accumulation and Production of Europe's Hydrocarbons III: Special Publication of the European Association of Petroleum Geoscientists No. 3. Springer, pp. 345-356.

Voskov, D., Abels, H., Vardon, P., et al.: A research and production geothermal project on the TU Delft campus, 49th Stanford Geothermal Workshop, Stanford University, Stanford, CA (2024).

Voskov, D.V.: Operator-based linearization approach for modeling of multiphase multi-component flow in porous media, Journal of Computational Physics, 337, (2017), 275-288.

Wang, Y., Voskov, D., Khait, M., et al.: An efficient numerical simulator for geothermal simulation: A benchmark study, Applied Energy, 264, (2020), 114693.

Wang, Y., Voskov, D., Khait, M., et al.: Influential factors on the development of a low-enthalpy geothermal reservoir: A sensitivity study of a realistic field, Renewable Energy, 179, (2021), 641-651.

Willems, C.J., Vondrak, A., Mijnlieff, H.F., et al.: Geology of the Upper Jurassic to Lower Cretaceous geothermal aquifers in the West Netherlands Basin–an overview, Netherlands Journal of Geosciences, 99, (2020), e1.

Wu, H., Fu, P., Hawkins, A.J., et al.: Predicting thermal performance of an enhanced geothermal system from tracer tests in a data assimilation framework, Water Resources Research, 57(12), (2021), e2021WR030987.